3D PRINTING AND ADDITIVE MANUFACTURING
Volume 2, Number 3, 2015

DOI: 10.1089/3dp.2015.0021

ORIGINAL ARTICLE

Additive Manufacturing of Optically Transparent Glass

John Klein,[1,*] Michael Stern,[2,*] Giorgia Franchin,[3,*] Markus Kayser,[1] Chikara Inamura,[1] Shreya Dave,[2] James C. Weaver,[4] Peter Houk,[5] Paolo Colombo,[3,6] Maria Yang,[2] and Neri Oxman[1]

Abstract

We present a fully functional material extrusion printer for optically transparent glass. The printer is composed of scalable modular elements able to operate at the high temperatures required to process glass from a molten state to an annealed product. We demonstrate a process enabling the construction of 3D parts as described by computer-aided design models. Processing parameters such as temperature, which control glass viscosity, and flow rate, layer height, and feed rate can thus be adjusted to tailor printing to the desired component, its shape, and its properties. We explored, defined, and hard-coded geometric constraints and coiling patterns as well as the integration of various colors into the current controllable process, contributing to a new design and manufacturing space. We report on performed characterization of the printed materials executed to determine their morphological, mechanical, and optical properties. Printed parts demonstrated strong adhesion between layers and satisfying optical clarity. This molten glass 3D printer demonstrates the production of parts that are highly repeatable, enable light transmission, and resemble the visual and mechanical performance of glass constructs that are conventionally obtained. Utilizing the optical nature of glass, complex caustic patterns were created by projecting light through the printed objects. The 3D-printed glass objects described here can thus be extended to implementations across scales and functional domains including product and architectural design. This research lies at the intersection of design, engineering, science, and art, representing a highly interdisciplinary approach.

Introduction and Background

ADDITIVE MANUFACTURING (AM) has undergone significant developments since its conception, as documented by Charles Hull in his patent of 1984 for the construction of parts using a photo-crosslinkable polymer.[1] Numerous processes have since been introduced, as summarized by the American Society for Testing and Materials, which defines seven categories according to which the wide range of processes can be classified.[2] Each of the various approaches relies on different physical characteristics and phenomena and is often associated with specific materials.

Throughout the history of manufacturing, the design process has often been guided by the constraints of the fabrication method. Current freeform fabrication capabilities enable a more flexible design space: fewer design constraints provide entirely new opportunities for the construction and assembly of objects at different length scales. Specifically, additional complexity in product scale is now possible without negatively affecting its production rate, cost, or quality. Furthermore, AM allows for simple, rapid, and economic design iteration, capitalizing on the efficacy of nonlinear design and optimization.

Extruded material built in three dimensions has proved its commercial value with the development of an entire consumer-level industry based on the principles of fused deposition modeling (FDM).[3] However, FDM printers, in their current embodiment, are unable to handle high-melting-point materials, and require feeding the material in filament form, thereby presenting significant limitations in size and scale.[1]

Two 3D printing methods are typically used for materials that require high temperature processing, such as metals and

[1]Media Lab, [2]Department of Mechanical Engineering, and [5]Department of Material Science and Engineering Glass Lab, Massachusetts Institute of Technology, Cambridge, Massachusetts.
[3]Department of Industrial Engineering, University of Padova, Padova, Italy.
[4]Wyss Institute for Biologically Inspired Engineering, Harvard University, Cambridge, Massachusetts.
[6]Department of Materials Science and Engineering, The Pennsylvania State University, University Park, Pennsylvania.
*These three authors have contributed equally to this work.

ceramics. The first one consists of a sintering method where particles are fused together below the melting point temperature. Parts are generally printed via binder jetting on a powder bed, where a binding agent temporarily joins particles until they are sintered through bulk thermal treatment.[4] The second method uses a laser (selective laser melting, SLM) or another thermal source to melt material particles that are either injected or present on the building platform.[5,6]

Glass-based materials hold the potential to provide particular value in the AM field due to their hardness, optical qualities, affordability, and availability. Research carried out to date on the AM of glass has been overall limited. Two main technologies have been applied; however, they both have substantial drawbacks. Binder jetting approaches have been applied to glass materials in order to overcome their high melting temperatures and high viscosity.[4,7,8] Sintered glass objects printed in this method are commercially available, but they are extremely fragile and appear opaque due to the light scattering from glass powders caused by incomplete densification.[9]

Moreover, even the most recent experiments with glass SLM have not been able to overcome such issues: products remain opaque and show poor mechanical properties. Furthermore, polishing requires extensive effort and access to all geometry and often results in the samples breaking into smaller pieces. Even when successful, internal porosity leads to significant light scattering, thus limiting transparency when implementing this method.[10] A manual wire feeding approach described in the same work yielded higher quality results; however, lack of automation limits control and prohibits part production.

Robocasting has also been investigated for the manufacturing of glass components, with particular interest in Bioglass® formulations for bone tissue engineering. In this process, glass particles are suspended in an aqueous solution or incorporated into a binder matrix. The mixture is then extruded through a nozzle to form a porous green body. As the green body undergoes sintering, however, it encounters the same limitations of the binder jetted glass parts described previously.[11–13]

The extrusion of molten glass, which appeared as early as the Mesopotamian period, remained in traditional glass manufacturing practices. In fact it is still applied in the artistic milieu: commercial kiln packages such as Bullseye Glass Co.'s Vitrigraph enable glass artisans to create glass canes or stringers through manual glass extrusion ranging in diameter from fractions of a millimeter to several millimeters.[14]

Large-scale manufacturing processes have also been developed for glass extrusion; they are particularly suitable for glass characterized by a narrow working temperature range and a relatively high softening point, such as silica glass (softening point $\sim$1600°C) or with a strong tendency to crystallize such as borosilicates. The application of pressure to force glass flow through a dye extends the glass working range to higher viscosities, and enables the production of rods and tubes with complex sections.[15] In this article, the development of tools and processes, which culminated in the first of its kind *fully functional material extrusion system for optically transparent glass,* is presented. This enabling technology and related platform is composed of scalable modular elements able to operate at the high temperatures required to process glass from the molten state to the final annealed product. Automated extrusion of 10-mm-diameter glass beads with a build rate of about 460 mm^3/s enabled the creation of 3D parts as described by computer-aided design (CAD) models with a build volume of 250 mm $\times$ 250 mm $\times$ 300 mm. The AM system and printed parts provide proof of concept for automated glass deposition and the ability to produce objects within an expansive design space. This method enables production of parts that are highly repeatable, allow light transmission, and resemble glass as conventionally produced. Printed components can be modular and scalable from artistic products to architectural constructions, as it can be seen by the examples included herein.

System Design and Construction

System implementation

The apparatus design and construction was guided by a series of successive tests with increasing complexity and control. They served as demonstration of operation of the printer and are briefly presented below to illustrate the evolution (see Table 1).

Initial tests were conducted using a previously heated ceramic crucible; molten glass was added and a slow flow was observed through the hole at the base. The tests proved that gravity-driven feed was feasible, but suggested that heating of the feed material would be critical. The second step involved the addition of a kiln surrounding the crucible during the process; glass flow of continually heated feed material was demonstrated. Flow was continuous and the glass was allowed to coil autonomously, forming tapered cylindrical shapes.

Computer control of the Z axis was then implemented, which enabled the system to maintain constant deposition height and to produce coiled cylinders with constant diameters. To create the first designed shape, bumpers were mounted on the frame and the crucible kiln was manually moved, successfully producing a square cross-sectional object. Digital control on the X and Y axes was then added, and more complex shapes were successfully fabricated. Implementation of software and motion control also provided the chance to set a constant travel speed. A rectangular prism being printed with this setup is presented in Figure 1A.

Despite the motion system reaching satisfactory mechanical control and precision, the printed parts showed inconsistent filament diameter, poor adhesion between layers, and rapid accumulation of defects. These problems derived from a common cause: the fact that glass was dripped from an offset height. An independently heated ceramic nozzle to be attached to the crucible was therefore designed and produced; with the nozzle tip below the carriage level, it was possible to print with no offset height. With this upgrade, control of the layer height was achieved and the above-mentioned issues were overcome. A cylinder being printed after the addition of the nozzle is shown in Figure 1B.

Glass objects need to be cooled down to room temperature in a slow and controlled way through the glass transition

Table 1. Glass 3D Printer Evolution Steps

1	Gravity feed proof of concept
2	Kiln autocoiling, fixed Z
3	Kiln autocoiling, moving Z
4	Kiln manual XY control
5	Kiln automatic control
6	Nozzle
7	Annealing chamber

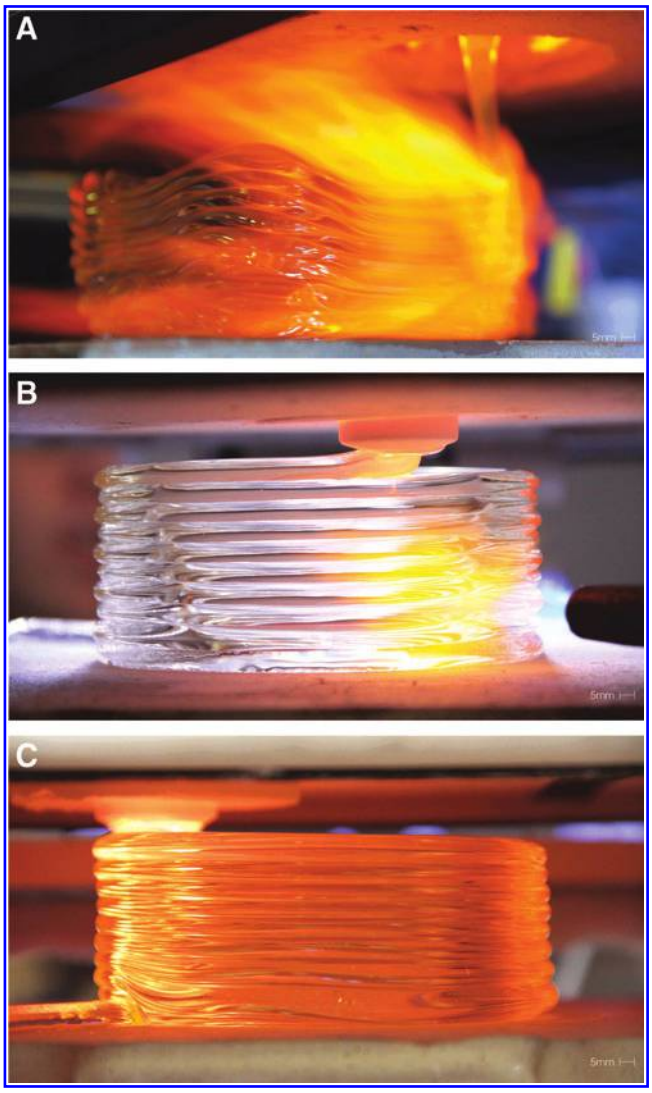

FIG. 1. Evolution of the printing process from its early stages **(A)**, through the introduction of a nozzle **(B)** to the current setup with an annealing chamber **(C)**.

temperature range, the annealing process, to release permanent stresses associated with thermal gradients that otherwise would lead to the spontaneous breakage upon cooling. The 3D-printed parts were kept above the annealing temperature (T_a) with the help of propane torches (visible in Fig. 1A and B) and were annealed right after the printing completion; the torching process was not automated and difficult to control, and therefore often the objects cracked. Finally, the introduction of a heated build chamber enabled *in situ* temperature control. Figure 1C shows the same build as in Figure 1B, this time being printed directly into the heated build chamber, providing consistent annealing temperature and eliminating the need for torches. The final setup resulted in a fully automated process and the capability to produce larger and stronger parts.

Hardware

Heating elements. The primary components of the system were the kiln cartridge (which contains a crucible kiln and nozzle kiln) and the print annealer (heated build chamber). A schematic of the whole assembly is shown in Figure 2A.

Inside the kiln cartridge (Fig. 2B), the crucible kiln (Fig. 2C) was an 1800 W high-temperature furnace that was used to melt and maintain molten glass at a temperature of 1040–1165°C. The kiln was made of alumina–silica fiberboard and it was heated through an FeCrAl coiled wire. Temperature was monitored via a type K thermocouple.

The nozzle kiln (Fig. 2D) was mounted to the bottom plate of the crucible kiln and provided 300 W of heat to the printer nozzle. The kiln was constructed similarly to the crucible kiln. Temperature was monitored via a type S thermocouple for faster response times. Each component of the system was a modular unit, to allow quick development. All heating elements and thermocouples exited out to a single area in the kiln cartridge, reducing limitations on the printer movements.

Glass was contained in a refractory crucible placed inside the crucible kiln; the nozzle kiln provided control over the flow of glass. The crucible included a bottom hole where the nozzle was inserted; the assembly was then sealed with a refractory mortar. The nozzle was machined from bulk high-temperature alumina bisque ceramic rods. The small dimensions of the nozzle allowed it to protrude below the carriage into the annealing chamber and enabled the direct deposition of glass with a precise control on layer height.

The glass was printed directly into the print annealer, which maintained a temperature above the glass transition temperature 480–515°C. The print annealer remained stationary while the *Z*-platform moved inside it. The *Z*-platform was fabricated out of a ceramic kiln shelf that enabled good initial bonding at high temperature and release at annealing temperature. The *XY* control was achieved by driving the print head. The 3300 W print annealer had two alumina–silica fiberboard doors to provide access to the nozzle and for removing the printed part, and a transparent ceramic (Neoceram®) window that enabled monitoring of the print job. The annealing chamber was based on the GlazeTech kiln (Skutt Kilns, Portland, OR).

The sealing of the annealing chamber was achieved through the addition of two light and thin alumina–silica fiberboard skirts, assuring that the annealing chamber was always closed on the top. One skirt was mounted on top of the annealing chamber, and the other to the moving carriage below the feed kiln.

Frame and carriage. The printer was constructed of 80/20 (80/20 Inc., Columbia City, IN) aluminum stock and square steel tube. Aluminum was used for components not exposed to high heat, while the heavier steel was reserved for central components that may become hot from the crucible kiln, print annealer, or radiating molten glass. The crucible kiln carriage consisted of steel supports mounted on bearings that traveled on the structural steel tracks. The entire system was mobile, mounted on pneumatic casters to enable transportation without damaging the fragile ceramic kilns.

Motion control. *XYZ* motion was provided by three independent stepper motors—lead screw gantry systems and drivers that were electronically controlled by an Arduino and a RAMPS 1.4 Arduino shield. The motors had a rated holding torque of 280 N·cm; the high torque was required due to the inertia of the kiln cartridge and carriage assembly.

The motors were connected to ACME lead screws with flexible helical couplings to accommodate misalignments. The motors were isolated from axial and radial loads by bearing blocks. The *Z* motor was mounted at the base of the

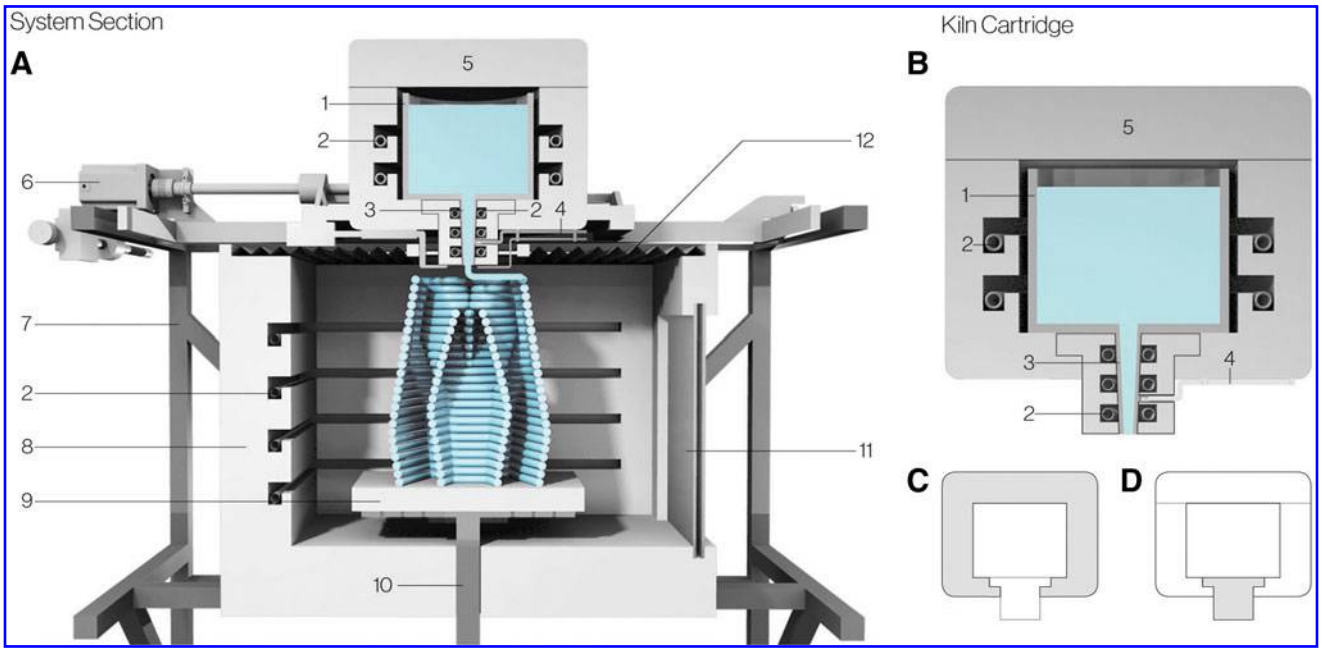

FIG. 2. Rendered cross section of the system showing **(A)** the printer during fabrication, **(B)** the kiln cartridge, **(C)** the crucible kiln, and **(D)** the nozzle kiln. Detail elements are as follows: (1) the crucible, (2) heating elements, (3) the nozzle, (4) the thermocouple, (5) removable feed access lid, (6) stepper motors, (7) printer frame, (8) print annealer, (9) ceramic print plate, (10) *z*-drive train, (11) ceramic viewing window, and (12) insulating skirt.

frame requiring only one hole at the base of the print annealer to accommodate the build platform support rod. Limit switches were mounted at the ''zeros'' of the *X*, *Y*, and *Z* axes both to provide homing information to the control software and to protect the system from mechanical crashes. These prevented the motor from driving when activated and were connected directly to the RAMPS board. The limit switch cables were bundled separately from the motor cables to prevent interference.

Software

CAD model. The 3D object was defined in Rhinoceros 5.0 environment. The model had to fit within the build chamber, that is, 250 mm × 250 mm × 300 mm. The input surface was described as a nonuniform rational basis spline (nurbs) geometry.

Slicing and generating G-code. The surface was sliced using a custom C# script in Grasshopper Build 0.9.76.0. The slicing script drew a helix around the CAD model structure, enabling continuous flow and accommodating for the specific filament diameter of extruded glass. This toolpath was then represented in Cartesian coordinates in the form of G-code. The layer height, curve discretization, and feed rate could be modified in real-time, while the tool path could be monitored in the preview pane. Users could also define specific velocities for each point. The algorithm developed for the wrapping toolpath started from the input surface, intersected it based on the layer height, discretized each intersection curve based on the input resolution, and then incrementally remapped the discretized points with increasing *Z* values. The remapped points were then connected with a polyline to create the continuous wrapping toolpath for any given complex geometry.

Motion control. G-code files were imported into the open source printing software Repetier-Host V1.0.6. Repetier firmware, adapted for the acceleration, velocities, and size of the build platform, was used to direct the printer.

System Operation Characterization

Material characterization

Commercial soda-lime glass nuggets (System 96® Studio Nuggets™; Spectrum® Glass Company, Inc., Woodinville, WA) were used in this study.

Glass density and thermal expansion coefficients (CTE) at low ($T \leq 210$°C) and high ($T = 1000$°C) temperature were estimated based on the glass composition. Fluegel models[16,17] were applied. Data are provided in Table 2.

Glass dynamic viscosity η strongly depends on temperature; its dependence can be modeled using the so-called Vogel–Fulcher–Tammann (VFT) equation[18–20]:

$$\log \eta(T) = A + \frac{B}{T - T_0} \tag{1}$$

Table 2. System 96® Studio Nuggets™ Density and Thermal Expansion Coefficients Estimations at Different Temperatures

Density and CTE	
T_0 (°C)	20
ρ_0 (g/cm^3)	2.53
T_1 (°C)	210
CTE_1 ($\times 10^{-6}$ K^{-1})	9.8
T_2 (°C)	1000
ρ_2 (g/cm^3)	2.34
CTE_2 ($\times 10^{-6}$ K^{-1})	32

CTE, thermal expansion coefficients.

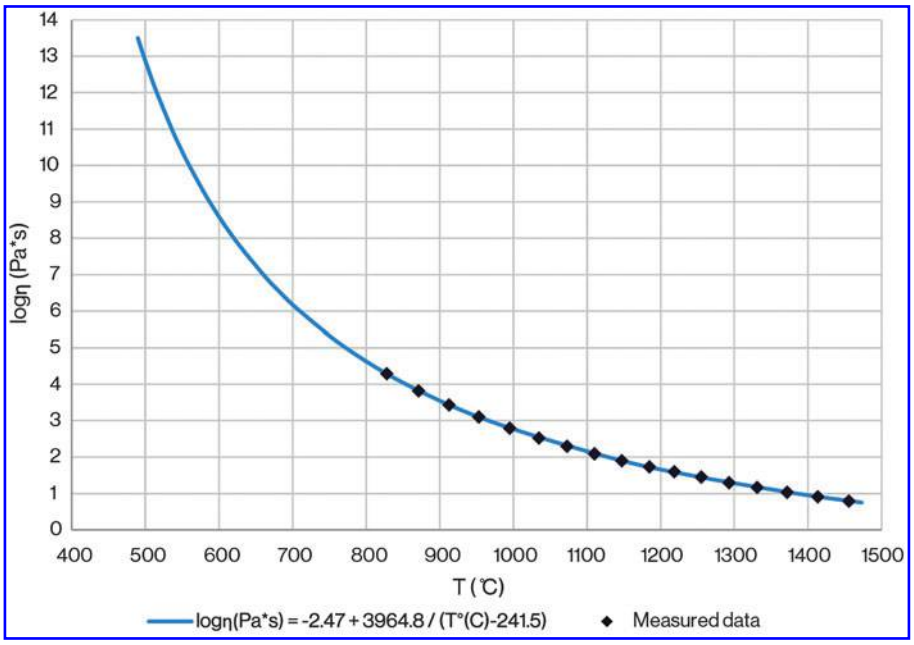

FIG. 3. Experimental viscosity data and resulting Volger-Fulcher-Tammann (VFT) equation.

where η (Pa·s) is the dynamic viscosity of the glass, T (°C) is its temperature, and A, B, and T_0 are experimental values depending on the glass composition.

Viscosity values were measured at different temperatures at Corning Inc. (Corning, NY) with proprietary equipment. Experimental data were fitted using the Volger-Fulcher-Tammann (VFT) equation to estimate A, B, and T_0, leading to the results shown in Figure 3. The VFT equation enables prediction of glass viscosity at each temperature, thus allowing flow estimation and process tailoring.

Process characterization

Temperature distribution. Based on glass viscosity data, the operating temperature was set at approximately 1000°C, corresponding to the glass working point ($\eta \sim 10^3$ Pa·s).

The nozzle temperature was set at $T = 1010$°C to account for the heat loss in the tip exposed to the annealing kiln environment.

The crucible temperature was set at $T = 1040$°C to overcome the heat loss due to frequent refilling.

The annealing chamber was set at $T = 480$°C, slightly below the glass annealing temperature (~ 515°C), because the glass heat radiation contributed to increase the environment temperature.

The temperature distribution in the system was simulated using Solidworks® Flow Simulation Computational Fluid Dynamics (CFD) software. Glass and refractories thermal properties were set as standard float soda-lime glass and 96% alumina, respectively.

Results are shown in Figure 4A.

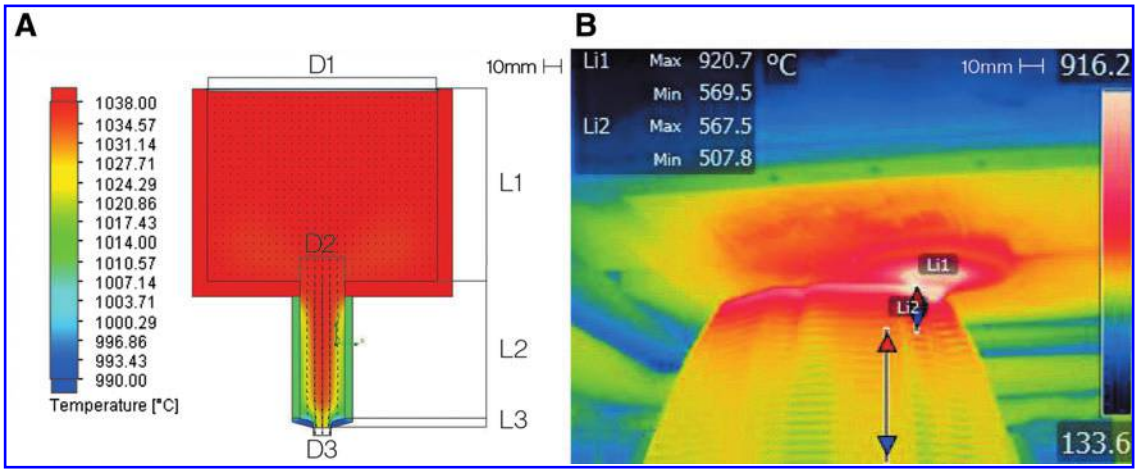

FIG. 4. Temperature distribution as observed in the printing platform: **(A)** Solidworks® simulation of the crucible and nozzle assembly (with diameters and lengths of different sections highlighted) and **(B)** thermal image of an object being printed (Image Credit: Forrest Whitcher).

Based on the CFD model, the temperature of the nozzle's outer face was expected to drop down to an average 980°C; the glass average temperature at the nozzle exit was 990°C.

Infrared images (Fig. 4B) were acquired from the heated chamber window during a printing process using a FLIR T335 equipped with a T197000 high-temperature option and were analyzed using FLIR Tools software (FLIR® Systems, Inc., Cambridge, MA). At the nozzle exit, glass temperature was observed to be 920°C, in agreement with the simulations. Temperature decreased drastically as new layers were deposited, creating a temperature gradient of ~350°C between the most recent five layers. This led to a viscosity increase of five orders of magnitude. This rapid increase in viscosity was crucial to the stability of the object during printing. Note that the object always remained in the 500–570°C temperature range, which corresponds to the annealing temperature of the glass in use; therefore, no cracks were formed during printing.

Physics of glass flow. The precise speed at which glass flowed through the nozzle was an important determining factor for feed rate calibration, helping to avoid undesired accumulation or lack of material on the printed object.

Glass flow through the nozzle can be modeled as laminar flow of a viscous fluid through a tube.[21] Whether a fluid under certain conditions will flow in a turbulent or laminar motion is a function of its density ρ (kg/m^3) and dynamic viscosity η (Pa·s) combined with its mean velocity v (m/s) and the channel diameter d (m); Reynolds number Re is a dimensionless parameter that combines these factors and is used to help predict similar flow patterns in different fluid flow situations. Flow is assumed laminar if its Re falls below a threshold value of 2040.[22]

In this case,

$$Re = \frac{\rho \times v \times d}{\eta} \sim 2.1 \times 10^{-4} \quad (2)$$

The assumption of laminar flow was therefore largely justified; moreover, $Re \ll 1$ also indicates that viscous forces were predominant over inertial ones (Stokes flow).[21]

The flow resistance of a tube is defined from the following relationship:

$$Q = \frac{\Delta P}{R} \quad (3)$$

where Q (m^3/s) is the volume flow rate through the tube, ΔP (Pa) is the pressure drop at the top of the nozzle, and R [Pa/(m^3/s)] is the resistance to flow.

ΔP is given by the glass weight; for a cylindrical crucible,

$$\Delta P = \rho g \Delta h \quad (4)$$

Q can also be expressed by

$$Q = A\frac{v_m}{2} = \frac{\pi r^4}{8\eta L}\Delta P \quad (5)$$

where A (m^2) is the nozzle opening surface area, v_m (m/s) is maximum flow velocity (at the center of the tube) and is two times the effective velocity, L (m) is the nozzle length, and r (m) is its radius. The equation is known as the Hagen–Poiseuille law.[21]

Table 3. Flow Resistance in the Crucible and Nozzle Assembly

	L *(mm)*	D *(mm)*	R *[Pa/(m^3/s)]*	R *(%)*
1	100	120	8.23×10^5	0.1
2	73.5	23.5	4.11×10^8	44.5
3	3	10	5.12×10^8	55.4
Total	176.5	—	9.24×10^8	—

R can therefore be calculated from

$$R = \frac{8}{\pi}\eta\frac{L}{r^4} \quad (6)$$

There are two factors that determine the resistance to flow within the nozzle: geometry (primarily the nozzle's radius) and glass viscosity.

Flow estimation. Based on previous equations, glass volumetric flow was estimated for typical processing parameters. Glass temperature at the nozzle exit was considered to be $T \sim 990$°C, corresponding to a dynamic viscosity $\eta \sim 640$ Pa·s.

The pressure drop was a function of the molten glass level inside the crucible, since the process was gravity driven. The crucible–nozzle assembly is outlined in Figure 4A. Designed lengths and diameters of crucible (1) and nozzle segments (2 and 3), along with correspondent flow resistances, are summarized in Table 3.

Based on the knowledge that the final smallest diameter drives the overall flow resistance, the length of the final segment was minimized. Table 3 shows that more than 50% of the flow resistance (R) was given by the final segment of the assembly.

For this calculation, it was assumed that at the start of a new print job the crucible was filled up to a height of $L' = 80$ mm, resulting in a pressure drop of $\Delta P \sim 3.6$ kPa. Volume flow rate at the nozzle exit was therefore $Q = 460$ mm^3/s with a consequent linear flow rate of $\bar{v} \sim 5.7$ mm/s.

As the glass level in the crucible decreased, Q and $\bar{v}$ decreased linearly; consistency during printing was achieved by frequent refilling of the crucible. The extended nozzle enabled direct deposition of material referenced from the machines Z height, rather than previous layer height; thus, any variation in flow rate would affect the wall width rather than the path height.

Fabrication of 3D-Printed Glass Parts

Method

Two methods for filling the crucible kiln were employed. In the first method, glass nuggets were heated in the crucible to 1165°C over 4 h; glass was then fined for 2 h to eliminate bubbles. During this phase, the nozzle was kept at a lower temperature ($T \sim 800$°C) to prevent glass flow. In the second method, molten glass was collected from a furnace and added directly to the crucible.

After fining, the crucible and nozzle temperatures were set to 1040°C and 1010°C, respectively. The print annealer was also set to 480°C. Glass flow typically initiated spontaneously due to gravity; however, flow could be terminated at the end of each print by cooling the nozzle tip with compressed air and reinitiated at the beginning of the following print by heating the nozzle tip with a propane torch.

Table 4. Annealing Cycle

Cooling rate (°C/h)	T *(°C)*	*Dwell time (h)*
—	480	1
25	400	—
50	150	—
50	80	—
120	20	—

Once the printing process was complete, the crucible and nozzle were drained by increasing their temperature up to 1165°C. The print annealer then executed the annealing cycle as summarized in Table 4.

For increased part production, other annealing kilns were used; objects were removed through the front door and placed in an external annealing kiln kept at 480°C until the end of the multiple printing session. They were then annealed following the same cycle.

Most objects were postprocessed in order to be properly displayed: sharp edges where the print was terminated were ground, and bottoms were polished to eliminate the roughness caused by the contact with the build platform during printing.

Parameters calibration and design space

Exploration of the forms developed had two unique objectives. The first was to identify the capabilities and limitations of our system; the second was to quantitatively characterize the most effective parameters to build successful parts. Parts printed during this process began as geometric primitives used for simple evaluation purposes. Prototypes rapidly evolved into objects that embodied capabilities such as the ability to print overhangs while also exploring a range of shapes and cross sections. The printed parts, in theory, could be made using traditional glass

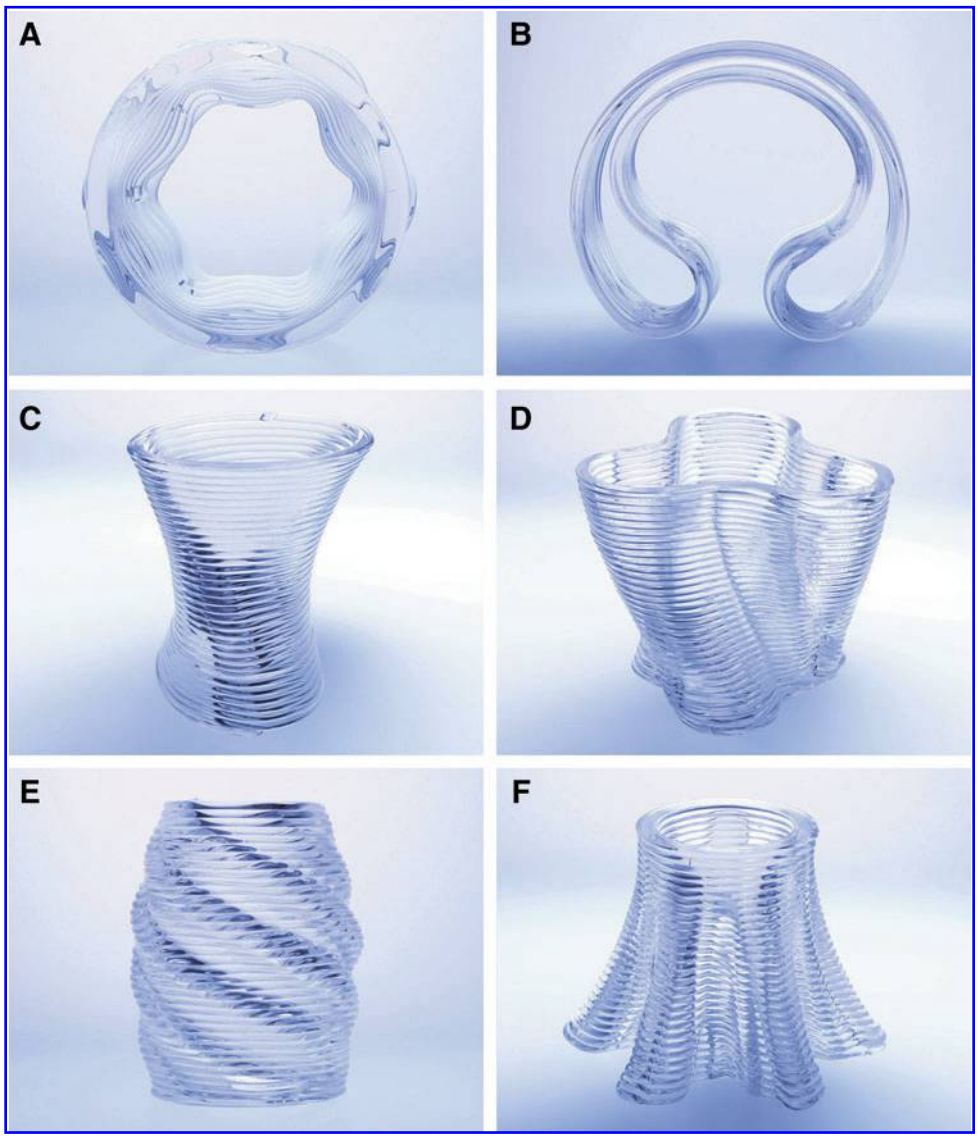

FIG. 5. Objects printed using the platform. **(A)** Parameters set (PS) 1, layer width. **(B–F)** PS 2, exploration of design space: **(B)** large radii, no drafting, focus on layer width; **(C)** smaller radii, higher drafting; **(D)** same as **(C)** but with changes in concavity/convexity in plane; **(E)** changes in concavity/convexity out of plane; **(F)** smallest radii and highest draft angles.

manufacturing methods, but would require complex and extremely expensive molds. Additionally, it would be impossible to generate optical surfaces without extensive polishing, a process in which expense is tied to formal complexity.

The printing process was tailored according to the temperature and resultant viscosity and flow rate. Greater detail on the printer parameters explored is presented below, expanding on the quantitative evaluation. Two different sets of parameters were used:

$T_{nozzle} = 1010°C$, layer height = 4.5 mm, feed rate = 4.5 mm/s

$T_{nozzle} = 1010°C$, layer height = 4.5 mm, feed rate = 6.1 mm/s

The first set of parameters was associated with a feed rate that was 20% slower than the estimated flow rate. This resulted in layers with a much larger width compared to the nozzle diameter; the average layer width of the printed parts was $w_1 = 19.5 \pm 3.5$ mm. A top view of a printed object is shown in Figure 5A. (Note: direct measurement of layer width was challenging; therefore, width was calculated based on the object's mass, layer height, feed rate, and printing time.)

Printing with this large layer width required a considerable amount of glass and therefore limited the design space. The second set of parameters was calibrated to achieve a smaller width, similar to the nozzle's orifice.

Different feed rates were tested in the range 5.8–6.3 mm/s, while keeping the other parameters constant. An optimum feed rate = 6.1 mm/s ($\sim$7% higher than the flow rate) was determined. Driving the extruder at a slightly greater rate than the natural flow helped achieve a more homogeneous filament, since the pulling prevented the buildup of any excess glass at the nozzle. In order to achieve effective adhesion of the first printed layer to the building platform, its feed rate was slowed down by 25%, eliminating the pulling force and giving the glass time to settle on the build platform. The second set of parameters resulted in an average width of $t_2 = 9.5 \pm 0.5$ mm, roughly half of what was produced with the first set. This approach enabled the production of larger and taller objects with the same amount of glass; the pressure head variation was more gradual and easier to control by frequent refilling. Figure 5B shows a top view of an object printed with the new set of parameters; Figure 5A and Figure 5B highlight the difference between layer widths.

Improved control achieved with the new set of parameters allowed for the exploration of various other possible designs. In the optimal printing conditions (clean nozzle, proper set of parameters), parts with draft angles up to 40° and turning radii down to 14 mm were printed.

The exploratory designs shown in Figure 5B–F (characteristics listed in Table 5) represent increasing levels of complexity and focus on different design objectives. The object in Figure 5B, for example, was not challenging in terms of minimum radius or draft angle, but investigated the possibility to fabricate thin channels and cavities by decreasing the distance between walls. Figure 5C shows a more complex object, with a minimum radius of 22 mm and a draft angle of 28°, which was successfully produced.

Working in a safe design space did not always produce defect-free objects. Radii and draft angles were not the only constraints that affected the quality of the print. Object in Figure 5D had a minimum radius of 28 mm and a draft angle of 29°; nevertheless, defects were observed in its bottom layers. It was determined that changes of convexity within the same layer often resulted in deviation from the CAD shape. This effect was caused by accumulation of glass on the nozzle tip and out-of-line pull force caused by surface tension between the glass on the nozzle face and the just deposited glass.

This phenomenon could be avoided by creating a geometry where the change in convexity occurred not within a single layer but instead over the height of the part: a successful example is shown in Figure 5E in comparison to that of Figure 5D.

The last object (Fig. 5F) was the most ambitious, printed with a minimum radius smaller than the nozzle diameter and abrupt changes in curvature. Deviations from the designed path followed a regular and repeatable pattern in the symmetric branches of the part.

Falling fluid deposition

Molten glass deposition from an offset may form a plethora of patterns when the relative speed of nozzle and substrate is lower than the impinging speed of the falling glass; those patterns include meanders, W patterns, alternating loops, and translated coiling. This phenomenon is of particular interest given the opportunity to fabricate multiscale objects where the features generated by coiling are at a much smaller scale than the motion of the printer. Viscous threading has been the subject of several studies involving a fluid falling on a moving belt and is often referred to as the ''Fluid Mechanical Sewing Machine.''[23–25] Brun *et al.*[26] recently developed a model to rationalize the rich variety of periodic patterns generated in terms of two parameters: the dimensionless height of fall H and the dimensionless velocity or travel speed V, which take into account the balance between gravitational stretching and viscous dissipation. For a thread, in this case glass, of kinematic viscosity ν (m^2/s) falling from a nozzle of

Table 5. Printed Objects: Parameters and Characteristics

	A	*B*	*C*	*D*	*E*	*F*
Nozzle *T* (°C)	1010	1010	1010	1010	1010	1010
Feed rate (mm/s)	4.5	5.8	6.1	6.1	6.1	6.3
Printing time (min)	22	39	34	39	37	44
Layer height (mm)	4.5	4.5	4.5	4.5	4.5	4.5
Calculated layer width (mm)	23	10	9	13	9	9
Min. radius (mm)	16	30	22	28	21	8
Max. draft angle (°)	20	0	28	29	28	32

FIG. 6. Falling fluid deposition: **(A)** deposition process (Image Credit: Steven Keating), **(B)** photographic detail of the printed object, and **(C)** a higher magnification 3D reconstruction from micro-computed tomography data.

dimensional height H^* onto a belt horizontally moving at speed V^*, it is

$$H = H^* \left(\frac{g}{v^2}\right)^{1/3} \tag{7}$$

$$V = \frac{V^*}{(vg)^{1/3}} \tag{8}$$

Based on this behavior, a cylinder with the following set of parameters was printed:

$T_{nozzle} = 1070°C$, layer height $= 4.5$ mm, feed rate $V^* = 6.1$ mm/s, offset height $H^* = 100$ mm, $H = 1.02$, and $V = 0.003$.

This resulted in the formation of a translated coiling pattern that followed the circular path to form a complex cylinder.

Details of the deposition process and of the object can be seen in Figure 6A and B.

The object was imaged by means of micro-computed tomography (micro-CT) with an XRA-002 X-Tek MicroCT (Xtek Inc., Cincinnati, OH) system in order to better visualize the generated patterns. The 3D reconstructions were performed using CT-Pro (Nikon Metrology Inc., Brighton, MI); surface renderings were generated using VGStudio Max (Volume Graphics GmbH, Heidelberg, Germany).

From the 3D reconstruction shown in Figure 6C, the generated loops seemed to be consistent in their radii and spacing.

Colored glass printing

Colored glass has been investigated since the very early stages of material exploration. One of the goals was to control the optical and esthetic properties of the printed glass structures through the integration of color. Preliminary tests demonstrated the effective printing with multiple glass colors in the same object.

Two variations of glass frits were used: Reichenbach R-19 Gold Topaz in F0 frit size (less than 1 mm), and R-11 Heliotrope in F2 size frit (2–4 mm) (Farbglashütte Reichenbach GmbH, Reichenbach, DE).

The frits were added in sequence to the crucible, which was partially filled with molten glass. Due to the relatively low melting point and mass, the frits melted within minutes. Figure 7 shows details of the resulting object. Both a sudden change and a graded conversion from one color to the other were possible within the same printed object. The printing process was not noticeably affected by addition of the colored frits.

Characterization of 3D-Printed Glass Parts

3D-printed cylinders were imaged via a micro-CT system (XRA-002 X-Tek MicroCT; Xtek Inc.) for quality purposes and were directly compared to their corresponding CAD files. 3D reconstructions were performed using CT-Pro (Nikon Metrology Inc.) and surface renderings of each cylinder were generated using the open source image processing package Fiji[27]; Rhinoceros 5.0 was used to evaluate each object's deviations from their CAD files.

Figure 8 shows a sectioned reconstruction from part of one such cylinder with its overlapping source file. The cylindrical prism design had a smooth surface with a constant outer diameter of 85 mm and a wall width of 9 mm; the actual cylinder, as expected, was composed of distinct layers as a result of the extrusion-based manufacturing process.

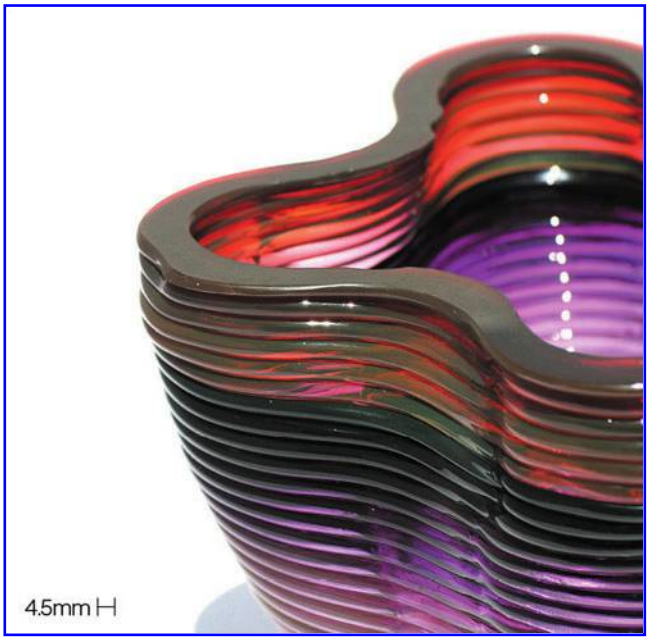

FIG. 7. Detail of a colored printed object. Both a sudden change in color (top ring) and a graded conversion (bottom) are visible.

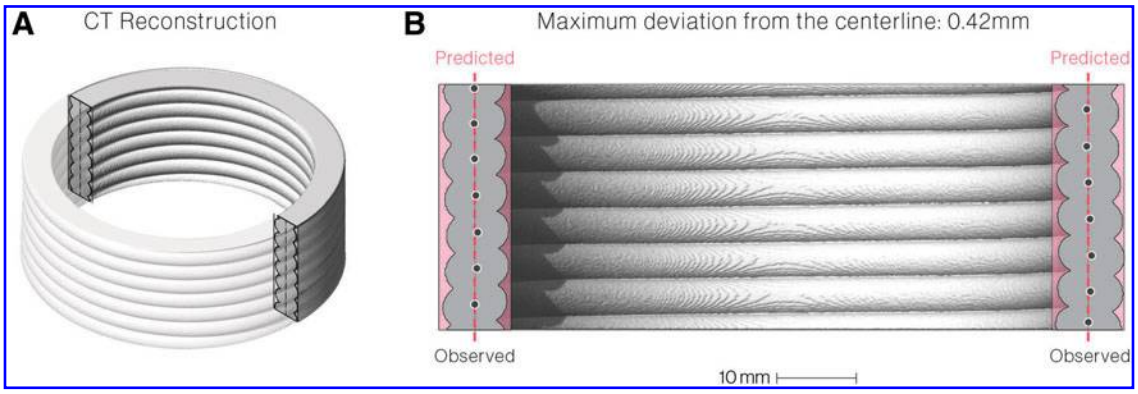

FIG. 8. **(A)** CT reconstruction of printed glass cylinder. **(B)** Cross section of printed glass cylinder showing deviation from the original computer-aided design file.

The layer height was 4.5 mm as per Gcode, and remained consistent through the analyzed six layers section, which was dictated by the direct deposition of the glass filament. The wall width was slightly but consistently overestimated in the CAD file; the average layer width was found to be 7.95 mm ± 0.19 mm; this variation was found to be a function of both head pressure based on glass level and nozzle orifice manufacturing tolerances.

The deposition of the glass layers, however, appears to be highly precise: the deviation of the filament centers from the centerline was 0.18 mm ± 0.13 mm over the analyzed section (or ca. 2.25% of the total wall thickness). The maximum deviation observed was 0.42 mm. Therefore, a conservative tolerance of 0.5 mm could be considered for the fabrication of glass printed objects using this approach.

In order to provide samples for optical and mechanical characterization, rectangular prisms were 3D printed and then cut down with a diamond saw. The cut surfaces were diamond ground and polished with cerium oxide.

A number of rectangular prisms were printed at room temperature (T_0) and then annealed; others were printed into the print annealer (T_a).

Samples were cut in different orientations: some of the bars (*a* in Fig. 9A) were cut with the longer axis along *Z* direction and others (*b*) with the longer axis along the *X* (or *Y*) direction. The samples height corresponded to the layer width. A representation of the samples and their specifications are shown in Figure 9A and Table 6, respectively.

Scanning electron microscopy

Samples were sputter-coated with gold and imaged with a Tescan Vega SEM (Tescan Orsay Holding, a.s., Brno-Kohoutovice, Czech Republic) and an FESEM Zeiss Ultra 55 (Carl Zeiss, Inc., Thornwood, NY). Images of an *a.Ta* sample are shown in Figure 9B and C.

The images demonstrate that the object's section was highly homogeneous with strong adhesion between the layers. Figure 9C shows an enlargement of the contact surface between two layers, with a smooth, blunt interface where no sign of the different layers was visible.

Residual stresses: polariscopy

The samples were observed under a Model 243 6'' Polariscope with Tint Plate (PTC® Instruments, Los Angeles, CA) to determine residual stress patterns developed during glass cooling.

Polariscopy is a well-known technique in glass industry as it takes advantage of stress-induced birefringence in glass to detect the presence of residual stresses mainly due to cooling gradients.[28,29] As polarized light travels through glass, it undergoes a delay proportional to the amount of stress. Therefore, color fringes visible through the analyzer mimic the stress pattern. Color and line intensity are not absolute, but depend on the orientation of the sample and the polarized filters. The results were obtained through qualitative reading of the color fringes with no quantitative evaluation of stress intensities.

Both samples printed at T_0 and T_a showed negligible stress concentration along the layers, indicating that the annealing treatment was successful. Looking at the cross sections, though, a difference between the two kinds of samples was detected. Printing at room temperature generated radial stresses within layers that had not been relieved by the subsequent annealing treatment. In the sample fabricated with the print annealer, on the other hand, such stresses were not present and the stress distribution was more homogeneous.

Preliminary mechanical testing

Residual stress patterns suggested that samples printed into the heated chamber possessed better mechanical properties compared to the ones printed at room temperature. The flexural behavior of the glass bars was investigated using an Instron 8841 and an Instron 5500R (Illinois Tool Works Inc., Glenview, IL) equipped with a 3-point bending fixture. Tests were performed at a cross-head speed of 0.05–0.12 mm/min. A compliant layer (Scotch® Permanent Outdoor Mounting Tape; 3M, Saint Paul, MN) was used between the bottom fixtures and the sample surfaces in some orientations. Results are reported descriptively due to the limited number of samples examined.

Figure 9D shows a sample loaded along the layers; this is usually the most critical loading configuration for a 3D-printed object, because delamination can occur due to a poor adhesion between layers.[30–32] The tests conducted on $a.T_0$ samples seemed to validate this hypothesis: the fracture occurred at the interface between two layers (Fig. 9E, left) and the samples possessed a flexural strength σ_f that was only one-fifth of the one of the annealed samples $a.T_a$. This was

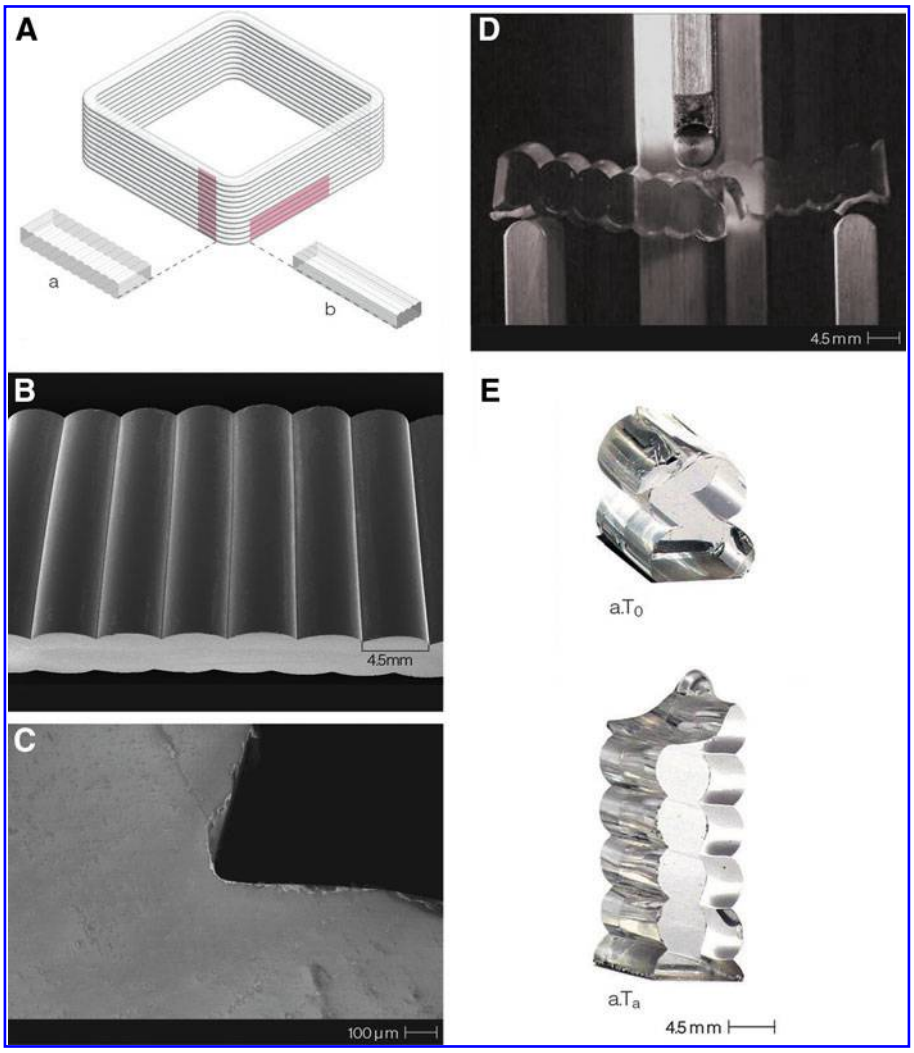

FIG. 9. Characterization of the printed parts. **(A)** Samples production from a printed prism. **(B)** SEM image of type a sample. **(C)** SEM image of the interface between two layers on a type a sample. **(D)** Three-point bending test on an $a.T_a$ sample (Image Credit: Kyle Hounsell). **(E)** Samples $a.T_0$ (left) and $a.T_a$ (right) after fracture. SEM, scanning electron microscopy.

most likely due to lower bonding strength caused by the large temperature difference between the deposited glass and the previous layer and to the presence of residual stresses between layers, as highlighted in the section Residual stresses: polariscopy. The absence of high residual stresses in $a.T_a$ samples resulted in fracture lines that propagated through a whole glass layer without following a precise trajectory (Fig. 9E, right), a further indication that no significant residual stresses were present in the sample.

TABLE 6. SAMPLES SPECIFICATIONS

	a.T_0	b.T_0	a.T_a	b.T_a
T (°C)	25		480	
Layer height (mm)	5.5		4.5	
Width (mm)	10.8 ± 0.8		9.8 ± 1.0	
Length (mm)	56.1 ± 1.8	78.0 ± 1.2	56.1 ± 1.8	78.0 ± 1.2
Base (mm)	17.7 ± 0.6	18.4 ± 0.4	17.7 ± 0.6	18.4 ± 0.4

Additionally, in the annealed samples flexural strength measured in the *a*- and *b*-type orientations differed by approximately 40%. This level of anisotropy is in line with what has been observed in plastic printed parts in other studies.[33]

Optical properties

One of the main goals of this work was to combine AM processes with the production of glass components possessing good optical properties.

Morphological and mechanical characterizations determined an overall high degree of homogeneity and good adhesion between layers, enabling light transmission with very little distortion. The 70-mm-tall cylinder shown in Figure 10A was polished with cerium oxide in both top and bottom layers; a high degree of transparency could be observed.

If layer surface texture was retained, it enabled light refraction and scattering as well as the production of highly complex caustic patterns. Images shown in Figure 10B were obtained by lighting the objects along their central axis using an LED.

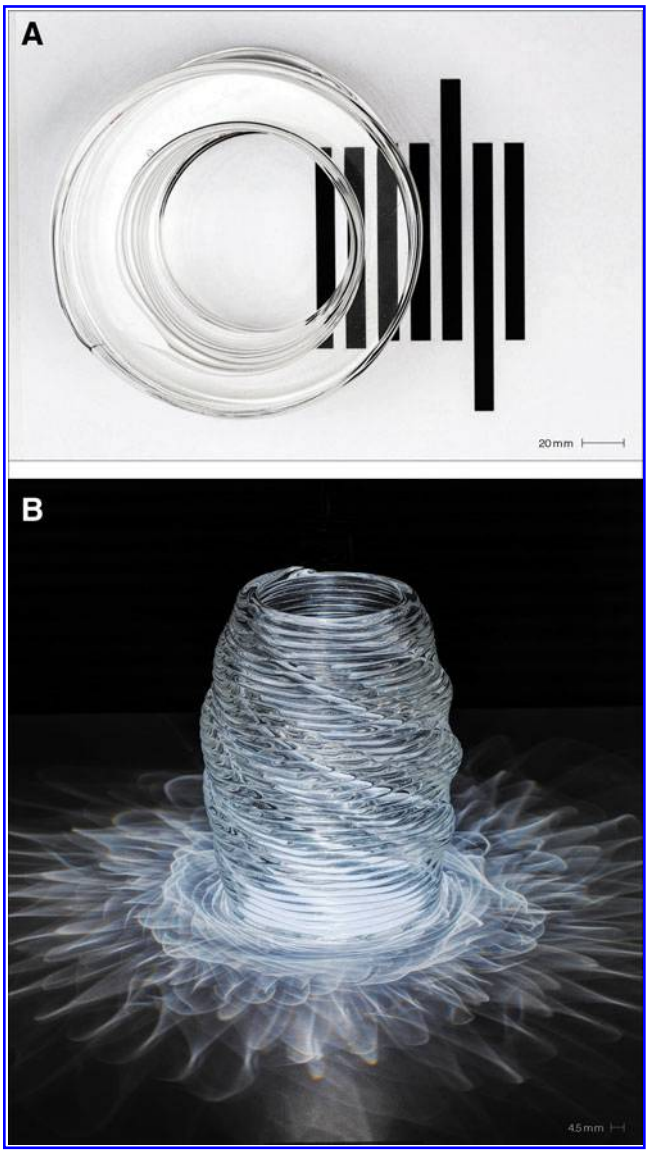

FIG. 10. Optical properties and caustic patterns of printed parts. **(A)** Top view of a 70-mm-tall cylinder showing a high level of transparency. **(B)** Caustic patterns created by illumination from a suspended overhead LED (Image Credit: Andy Ryan).

The observed behavior offered new perspectives on light control and additional optical properties for the printed objects. Work by Kiser *et al.* has shown that precomputed shapes can be generated with caustics by modeling light transmission to control the patterns and form desired shapes providing future directions for this work to explore.[34]

Limitations and Future Work

The focus of the present work was to demonstrate the functionality of a molten glass material extrusion system; initial work focused primarily on the printer construction and process calibration to this end. There are many different directions for future work that arise based on this first glass 3D printer.

Only preliminary testing was conducted on the printed glass objects. More comprehensive morphological, mechanical, and optical characterizations of printed components are underway and future work will validate the qualitative observations through more accurate and extensive testing.

The printer here presented is still in development and there are a number of improvements that are currently being carried out. For instance, extruded glass stuck preferentially on glass covering the nozzle tip instead of on the colder previous layer; such phenomenon was responsible for the deviation from desired shapes and uneven glass distribution. Future work on the printer will focus on solving this issue. Numerous potential solutions will be tested by creating new nozzle geometry, material, coating, face cooling, or the addition of sacrificial foil.

Software environment improvements will be explored to merge the large number of separate pieces of software needed to run the system. This will enable the operator to have full control of printing process in real time, including direct control over the kilns' temperatures and path modification and travel speed, from the same interface.

Gravity as a feed mechanism required frequent refilling of the crucible, needed to keep the glass level almost constant. This procedure affected the quality of the print—from nearly imperceptible to those observable with the naked eye. Having a continuous flow of material in the feeding chamber would allow the realization of more homogeneous parts.

The relatively small pressure drop generated by the gravity-fed system was also a limiting factor in terms of printing speed and resolution, and also prevented scaling down the nozzle diameter. Future development will therefore involve the addition of an active material feed system (in the form of a plunger or of compressed air) in order to increase control and enable a more diverse set of parts to be fabricated at a faster rate and with finer resolution.

The printer development was carried out using soda lime glass, chosen because of its relatively low working temperature and wide working range. Our method could be applied to a diverse range of materials, including other silicate, borate, and phosphate glasses as well as glass–ceramic systems. In order to process these materials, a future version of the printer would thus be able to heat glass to higher temperatures.

To fully achieve the level of complexity of AM processes, this system requires the ability to automatically start, stop, and cut the glass filament. In the current setup, these tasks are manually activated by the operator. Multiple different mechanisms to achieve this level of control are being explored from automating the compressed air and torching that currently performed manually to adding shears or a high-temperature valve. The addition of these features would expand the design space enabling the creation of designs with intricate cross sections and internal structures.

Initial research is being conducted to review the benefits of 3D printing glass technologies for architectural applications. A multifunctional building module can be created by coupling glass's properties (compressive strength, optical transparency, and chemical inertness) with the ability to deposit material in complex cross sections. Gutierrez and Lee[35] are investigating a building envelope for ''greywater reuse and integrated thermal (GRIT) building control,'' which treats greywater through a system of microlenses submerged in a microbial solution to create the photocatalytic treatment process. The optical properties exhibited from the printed glass structures can be further refined to concentrate light by customizing extrusion profiles.

Achieving light concentrating filaments would enable a façade system from assembled printed components that have filaments layered into structural tube networks to distribute heat, and treat fluids and air.

Conclusions

This article documents the development of the first molten glass material 3D extrusion system for the production of optically transparent components. This system processed glass from the molten state to annealed components of complex digitally designed forms. The printing parameters and process were optimized, enabling high repeatability and control.

Process optimization involved the addition of a ceramic nozzle of controlled geometry, modeling the glass viscosity, controlling glass levels, adjusting the temperature distribution in the different kilns, as well as varying more conventional printing parameters such as layer height and feed rate. The design space enabled by this system was mapped, including geometric constraints such as maximum overhang and minimum turning radius. Additionally, integration of colors was shown to be possible, and the generation of coiling patterns as a means to produce objects of multiple different length scales was investigated.

Preliminary printed material characterization was performed in terms of morphological, mechanical, and optical properties. Results indicated strong adhesion between layers and substantial strength increase when the process was performed in a heated build chamber with roughly 60% of material strength across layers. From the optical point of view, high transparency was observed and complex caustic patterns were created with LED light sources depending on the samples' geometry.

Two trends in AM highlight the value we expect from AM of molten glass. First, the freedom that this process provides in terms of the forms that can be created in glass enables the creation of structures characterized by higher structural and environmental performance delivered through geometric complexity. Currently, we are observing how geometrical complexity can be leveraged for engineering gain, particularly in the aerospace industry in some cases improving performance by 40% or more.[3,36,37] As designers learn to utilize this new freedom in glass manufacturing, it is expected that a whole range of novel applications will be discovered. Second, bespoke creation of glass objects provides the opportunity for complex scaffolds, fluidics, and labware custom made for individual applications. Moving forward, the simultaneous development of the printer and the design of the printed glass objects will yield both a higher performance system and increasingly complex novel objects. As such, applications in art, architecture, and product design will be further explored, while improvements such as continuous feeding, plunging, increased build size, and start and stop control will be implemented in parallel.

Acknowledgments

This research was primarily sponsored by the Mediated Matter research group at the MIT Media Lab. It was supported in part by the MIT Department of Mechanical Engineering through a project in the course additive manufacturing (2.S998) in spring 2014 and by the Glass Art Society through the Technology Advancing Glass Grant. G.F. was partially supported by a scholarship awarded by ''Fondazione Aldo Gini'' in Padova, Italy. We would like to thank Associate Prof. John A. Hart for his support of our work and for his technical advice. We would also like to thank Prof. J. Meejin Yoon, Department Head and MIT's School of Architecture and Planning, as well as Prof. John A. Ochsendorf from MIT's Department of Civil and Environmental Engineering and Prof. Neil Gershenfeld from MIT's Center for Bits and Atoms for their guidance and support. We thank Forrest Whitcher for collecting IR images; Mary Ann Babula for cutting, grinding, and polishing; Michael Tarkanian and Daniel Lizardo for their assistance with polariscopy and mechanical tests in the MIT Mechanical Behavior of Materials Lab; and Kyle Hounsell for recording high-speed videos during mechanical tests. We also wish to acknowledge Corning Incorporated for viscosity measurements and technical advice, as well as Skutt Kilns and Smart Ceramics for support during the printer design and building phases. In addition, we wish to thank Joi Ito, director of the MIT Media Lab, for his continuous support.

Author Disclosure Statement

Klein J, Franchin G, Stern M, Kayser M, Inamura C, Dave S, Oxman N, Houk P, Methods and apparatus for AM of glass, U.S. Patent Application 14697564, filed April 27, 2015. No other competing financial interests exist.

References

1. Gibson I, Rosen DW, Stucker B. Chapter 2: Development of additive manufacturing technologies. In: Additive Manufacturing Technologies: Rapid Prototyping to Direct Digital Manufacturing. New York: Springer Science + Business Media, LLC, 2010, pp. 17–40.
2. American Society for Testing and Materials. Standard Terminology for Additive Manufacturing Technologies. West Conshohocken, PA: ASTM, 2012.
3. Wohlers T, Caffrey T. Wohlers Report 2014. Fort Collins: Wohlers Associates, 2014.
4. Marchelli G, Prabhakar R, Storti D, Ganter M. The guide to glass 3D printing: Developments, methods, diagnostics and results. Rapid Prototyp J 2011;17:187–194.
5. Zocca A, Colombo P, Gomes CM, Guenster J. Additive Manufacturing of Ceramics: Issues, potentialities and opportunities. J Am Ceram Soc 2015;98:1983–2001.
6. Murr LE, Gaytan SM, Ramirez DA, *et al.* Metal fabrication by additive manufacturing using laser and electron beam melting technologies. J Mater Sci Technol 2012;28:1–14.
7. Fateri M, Khosravi M. On-site additive manufacturing by selective laser melting of composite objects. Concepts and Approaches for Mars Exploration, held June 12–14, 2012, in Houston, Texas. LPI Contribution No. 1679, id.4368.
8. Klein S, Simske S, Parraman C, *et al.* 3D Printing of Transparent Glass. HP Technical Report 2012. HP Laboratories, HPL-2012-198.
9. The ExOne Company LLC. The New Standard for Manufacturing from ExOne. Manufacturing in Sand. http://prometal.com/sites/default/files/brochures/X1_General_sellSheets.pdf (accessed Sept. 1, 2015).
10. Luo J, Pan H, Kinzel EC. Additive manufacturing of glass. J Manuf Sci Eng 2014;136:061024.
11. Clasen R. Method for the manufacture of glass bodies by extrusion. US Patent US4682995, 1987;2–7.
12. Clasen R, Schmidl B. Method of manufacturing glass bodies by means of extrusion. US Patent US4816051, 1989.

13. Eqtesadi S, Motealleh A, Miranda P, *et al.* Robocasting of 45S5 bioactive glass scaffolds for bone tissue engineering. J Eur Ceram Soc 2014;34:107–118.
14. Bullseye Glass Co. The Vitrigraph Kiln—Creating a New Vocabulary in Fused Glass. Portland, OR: Bullseye Glass Co., 2014, pp. 1–4.
15. Roeder E. Extrusion of glass. J Non Cryst Solids 1971; 5:377–388.
16. Fluegel A. Global model for calculating room-temperature glass density from the composition. J Am Ceram Soc 2007;90:2622–2625.
17. Fluegel A, Earl Da, Varshneya AK, Seward TP. Density and thermal expansion calculation of silicate glass melts from 1000°C to 1400°C. Phys Chem Glas Eur J Glas Sci Technol Part B 2008;49:245–257.
18. Vogel H. Das Temperaturabhängigkeitsgesestz der Viskosität von Flüssigkeiten. Phys Z 1921;22:645–646.
19. Tammann G, Hesse W. Die Abhängigkeit der Viskosität von der Temperatur bei unterkühlten Flüssigkeiten. Z Anorg Allg Chem 1926;156:245–257.
20. Fulcher GS. Analysis of recent measurements of the viscosity of glasses. J Am Ceram Soc 1925;8:339–355.
21. Bird RB, Stewart WE, Lightfoot EN. Transport Phenomena. New York: Wiley, 1958.
22. Reynolds O. An experimental investigation of the circumstances which determine whether the motion of water shall be direct or sinuous, and of the law of resistance in parallel channels. Phil Trans R Soc Lond 1883;174:935–982.
23. Chiu-Webster S, Lister JR. The fall of a viscous thread onto a moving surface: A ''fluid-mechanical sewing machine.'' J Fluid Mech 2006;569:89.
24. Ribe NM. Coiling of viscous jets. Proc R Soc A Math Phys Eng Sci 2004;460:3223–3239.
25. Ribe NM, Habibi M, Bonn D. Liquid rope coiling. Annu Rev Fluid Mech 2012;44:249–266.
26. Brun P-T, Audoly B, Ribe NM, *et al.* Liquid ropes: A geometrical model for thin viscous jet instabilities. Phys Rev Lett 2015;174501:1–5.
27. Schindelin J, Arganda-Carreras I, Frise E, *et al.* Fiji: An open-source platform for biological-image analysis. Nat Methods 2012;9:676–682.
28. Mastelaro VR, Zanotto ED. Residual stresses in a soda-lime-silica. J Non Cryst Solids 1996;194:297–304.
29. Preston FW. The use of polariscopes in the glass industry. J Am Ceram Soc 1930;13:595–623.
30. Belter JT, Dollar AM. Strengthening of 3D printed fused deposition manufactured parts using the fill compositing technique. PLoS One 2015;10:e0122915.
31. Ahn S-H, Montero M, Odell D, *et al.* Anisotropic material properties of fused deposition modeling ABS. Rapid Prototyp J 2002;8:248–257.
32. Bertoldi M, Yardimci Ma, Pistor CM, *et al.* Mechanical characterization of parts processed via fused deposition. Proceedings of the 1998 Solid Freeform Fabrication Symposium, 1998, pp. 557–565.
33. Kim GD, Oh YT. A benchmark study on rapid prototyping processes and machines: Quantitative comparisons of mechanical properties, accuracy, roughness, speed, and material cost. Proc Inst Mech Eng Part B Eng Manuf 2008; 222:201–215.
34. Kiser T, Eigensatz M, Nguyen MM, *et al.* Architectural caustics—Controlling light with geometry. Adv Archit Geom 2012;2013:91–106.
35. Gutierrez MP, Lee LP. Engineering multiscale design and integration of sustainable building functions. Science 2013; 341:247–248.
36. Airbus. Printing the Future: Airbus Expands Its Applications of the Revolutionary Additive Layer Manufacturing Process, 2014.
37. Edwards T. New Data Shows That 3D Printed Components Could Cut Aircraft Weight By 7 Percent. 2015. http://3dprint.com/71279/3d-print-aircraft-weight/ (accessed Sept. 1, 2015).

Address correspondence to:
Neri Oxman
MIT Media Lab
75 Amherst Street, E14-433B
Cambridge, MA 02139

E-mail: neri@mit.edu